Chemical Science

ROYAL SOCIETY OF CHEMISTRY

EDGE ARTICLE

View Article Online
View Journal | View Issue

Cite this: *Chem. Sci.*, 2024, **15**, 10172

All publication charges for this article have been paid for by the Royal Society of Chemistry

Received 19th January 2024
Accepted 26th May 2024

DOI: 10.1039/d4sc00454j

rsc.li/chemical-science

Tunable Pt–NiO interaction-induced efficient electrocatalytic water oxidation and methanol oxidation†

Fenglin Wang,[ab] Zhicheng Zheng,[b] Dan Wu,[b] Hao Wan, *[a] Gen Chen,[b] Ning Zhang, [b] Xiaohe Liu *[ab] and Renzhi Ma *[c]

Metal–support interaction engineering is considered an efficient strategy for optimizing the catalytic activity. Nevertheless, the fine regulation of metal–support interactions as well as understanding the corresponding catalytic mechanisms (particularly those of non-carbon support-based counterparts) remains challenging. Herein, a controllable adsorption–impregnation strategy was proposed for the preparation of a porous nonlayered 2D NiO nanoflake support anchored with different forms of Pt nanoarchitectures, *i.e.* single atoms, clusters and nanoparticles. Benefiting from the unique porous architecture of NiO nanosheets, abundant active defect sites facilitated the immobilization of Pt single atoms onto the NiO crystal, resulting in NiO lattice distortion and thus changing the valence state of Pt, chemical bonding, and the coordination environment of the metal center. The synergy of the porous NiO support and the unexpected Pt single atom–NiO interactions effectively accelerated mass transfer and reduced the reaction kinetic barriers, contributing to a significantly enhanced mass activity of 5.59 A mg_{Pt}^{-1} at an overpotential of 0.274 V toward the electrocatalytic oxygen evolution reaction (OER) while 0.42 A mg_{Pt}^{-1} at a potential of 0.7 V *vs.* RHE for the methanol oxidation reaction (MOR) in an alkaline system, respectively. This work may offer fundamental guidance for developing metal–loaded/dispersed support nanomaterials toward electrocatalysis through the fine regulation of metal–support interactions.

Introduction

Tremendous energy conversion technologies have been directed towards renewable energy sources and carbon neutralization, including water electrolysis and direct methanol fuel cells (DMFCs).[1] Hydrogen energy, the most eco-friendly renewable energy source, can be sustainably generated by conducting water electrolysis. However, the anodic multi-electron water oxidation (*i.e.* oxygen evolution reaction, OER) possesses sluggish kinetics manifested in a high energy barrier and overpotential,[2] which significantly affects the efficiency of the overall water splitting. Compared to hydrogen energy, renewable methanol serves as another commonly utilized fuel that can be easily stored and transported with existing infrastructure of petrol.[3] DMFCs represent a kind of remarkable energy conversion device for the high-efficiency utilization of reproducible methanol through the oxidization of fuel, realizing the direct conversion of chemical energy into electric energy.[4,5] Nevertheless, the development of effective anodic electrocatalysts for the sluggish methanol oxidation reaction (MOR, $CH_3OH + H_2O \rightarrow CO_2 + 6H^+ + 6e^-$) remains the bottleneck of DMFCs.[6,7] In addition, the MOR process involves a complex 6-electron transfer mechanism and multiple pathways, such as the CO-containing pathway or others, which severely depend on catalysts.[6,7] In this regard, it is challenging and of scientific significance to design electrocatalysts with high activities toward the OER and MOR.[8,9]

Precious platinum (Pt) has attracted great interest in the oxidation reaction field due to its intriguing physicochemical properties and unprecedented catalytic efficiency.[10,11] Strategies such as constructing ingenious geometrical nanostructures and modulating the Pt valence state are aimed at enhancing Pt utilization and electrocatalytic activity, but still remain challenging. Single-atom catalysts (SACs) have emerged as novel nanostructures with unique advantages in precisely controlling active sites, which is attributed to the exposure of numerous surface atoms, the tunable electronic structure and the coordinative environment.[12] The typical synthetic methods such as

[a]*Zhongyuan Critical Metals Laboratory, Zhengzhou University, Zhengzhou 450001, P. R. China. E-mail: wanhao@zzu.edu.cn; liuxh@csu.edu.cn*

[b]*School of Materials Science and Engineering, Key Laboratory of Electronic Packaging and Advanced Functional Materials of Hunan Province, Central South University, Changsha, Hunan 410083, P. R. China*

[c]*Research Center for Materials Nanoarchitectonics (MANA), National Institute for Materials Science (NIMS), Tsukuba, Ibaraki 305-0044, Japan. E-mail: MA.Renzhi@nims.go.jp*

† Electronic supplementary information (ESI) available: Experimental information, DFT calculations, XRD and SEM data, HAADF-STEM image, SAED pattern, HRTEM image, mass-normalized CV curves for the MOR. See DOI: https://doi.org/10.1039/d4sc00454j

impregnation, co-precipitation, sputtering and alloying have been employed for the doping of single atoms, showcasing the versatility and potential of SACs in catalysis.[13–16]

Notably, the catalytic activity of an entire SAC is closely dependent on the anchored substrate. Besides paying attention to single-atom center species, it is necessary to regulate the surrounding environment to achieve the optimal electronic structure and coordination by tuning the chemical bonds between single atoms and the substrate.[17–21] For example, Pt single atoms supported by carbon black or carbon nanotubes exhibit inert catalytic activity, whereas Pt single atoms immobilized on RuO_2 show superior catalytic mass activity and stability.[12,22] Thereby, the selection of substrates for SACs implies a complex and multi-perspective challenge in boosting the SAC activity toward the OER and MOR, such as alloys,[23] MoS_2,[15] MXene nanosheets,[24,25] metal nanoparticles[16,26] and transition metal oxides.[13] Notably, NiO is a promising substrate due to its facile phase transformation into highly active NiOOH with a layered double hydroxide structure during the catalytic oxidation process,[27] which is conducive to providing a migration channel for OER intermediates and thus facilitating the oxidative removal of CO_{ads} on the activity sites in the MOR.

Recently, metal–support interactions, mainly those between metals and carbon substrates, have been massively studied for enhancing the electrocatalytic performance. For instance, Pt single atoms loaded on thiolated multiwalled carbon nanotubes are barely significant to the MOR catalytic activity, while Pt clusters possess a small MOR overpotential,[28] attributed to the requirement of at least three Pt atoms to form a combined active site for the MOR.[29] The dispersion and size of Pt are vital factors in determining the metal–support interactions and thus optimizing the electrocatalytic activity. Considering that single atoms predominantly anchor on the surface of materials, the charge state and distribution of SACs on the support directly influence Gibbs free energies of the crucial intermediates involved in the catalytic process, thereby tuning the rate-determining steps involved in the OER and MOR. Hence, regulating the noble metal–NiO support interactions by controlling the metal size and nanoarchitecture is an effective approach to modulate the electronic structure and bonding state around single atom-based catalysts.

Herein, a facile adsorption–impregnation strategy was employed to adjust the light condition and reaction time, facilitating the immobilization of different Pt nanostructures (single atoms, clusters, and nanoparticles) on the porous NiO nanoflake substrate, and thus achieving NiO–Pt single atoms (NiO–Pt_{SA}), NiO–Pt clusters (NiO–$Pt_{cluster}$) and NiO–Pt particles (NiO–$Pt_{particle}$) respectively. The porous architecture of 2D nonlayered NiO offered abundant defects and accelerated mass transfer. The metal–NiO interactions and their effects on the catalytic performance were systematically studied. Remarkably, the immobilized Pt single atoms effectively reduced the reaction kinetic barrier and enhanced the catalytic activity in an alkaline system. As a result, the as-constructed NiO–Pt_{SA} catalyst displayed high OER performance with an enhanced mass activity of 5.59 A mg_{Pt}^{-1} at a current density of 10 mA cm^{-2}, and an enhanced MOR peak mass activity of 0.42 A mg_{Pt}^{-1} at 0.7 V *vs.* RHE.

Results and discussion

Diverse Pt nanostructures (*i.e.* single atoms, clusters or nanoparticles) immobilized on a porous NiO nanosheet substrate were synthesized by a facile adsorption–impregnation method, as illustrated in Fig. 1A. First, α-type layered nickel hydroxide intercalated with anionic surfactant dodecyl sulfate (denoted as α-$Ni(OH)_2$-DS) was prepared *via* an oil bath process. The basal reflection series of the product well matched with a typical α-$Ni(OH)_2$-DS layered structure with an interlayer spacing of 2.6 nm (Fig. 1B(I)). A substantial quantity of uniform nanoflakes was observed in the representative scanning electron microscopy (SEM) image (Fig. 1C). Second, the influence of calcination temperature on the morphology and structure of the calcined product was investigated in detail. Interlayer anionic DS^- could not be completely removed at 600 °C (Fig. S1 and S2†), while pores would form and lead to morphological defects at a calcined temperature of 800 °C (Fig. S3 and S4†). Therefore, the optimal NiO with standard crystal (JCPDS No. 65-2901, Fig. 1B(II)) and porous nanosheet morphology (Fig. S5†) was obtained through calcination at an ambient temperature of 700 °C. The porous feature of the NiO nanoflakes was further confirmed by transmission electron microscopy (TEM) (Fig. 1D). A high-resolution TEM image (HRTEM) indicated

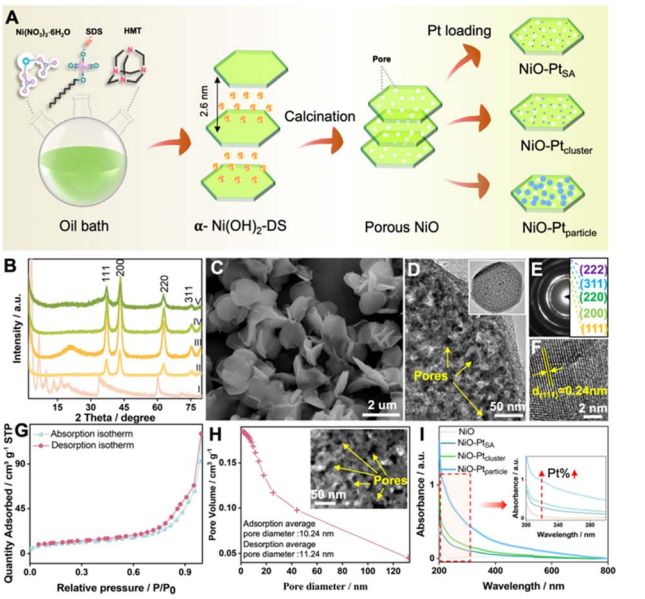

Fig. 1 Compositional and structural characterization of the porous NiO substrate and NiO–Pt_{SA}, NiO–$Pt_{cluster}$, NiO–$Pt_{particle}$. (A) Schematic illustration of the fabrication procedure for porous NiO–Pt_{SA}, NiO–$Pt_{cluster}$ and NiO–$Pt_{particle}$ catalysts. (B) XRD patterns of (I) α-$Ni(OH)_2$-DS, (II) porous NiO (calcined at 700 °C), (III) NiO–Pt_{SA}, (IV) NiO–$Pt_{cluster}$, and (V) NiO–$Pt_{particle}$. (C) SEM image of a-$Ni(OH)_2$. (D) TEM image, (E) SAED pattern and (F) HRTEM image of NiO. (G) BET isotherm of porous NiO. (H) BJH-plot of pore volume *vs.* pore diameter, the inset is a HAADF image of porous NiO. (I) UV-visible absorption spectra of NiO and the three NiO/Pt samples.

clear lattice fringes with a lattice space of 0.24 nm, corresponding to the (111) planes of NiO (Fig. 1F). The selected area electron diffraction (SAED) pattern, as shown in Fig. 1E, revealed the polycrystalline nature of NiO nanoflakes.

The surface properties of NiO were investigated by Brunauer–Emmett–Teller (BET) characterization. The isotherms of NiO showed a hysteresis loop with high relative pressure (P/P_0) in the range of 0 to 1 according to the N_2 adsorption–desorption isotherms (Fig. 1G), and the BET surface area for NiO was thus estimated as 36.99 m^2 g^{-1}. Based on the related pore size distribution plot by the Barrett–Joyner–Halenda (BJH) method, the pore size of NiO nanoplates was predominantly distributed between 1 and 20 nm. The average pore diameter for adsorption and desorption was 10.24 nm and 11.24 nm, respectively, as shown in Fig. 1H. The porous feature morphology of NiO may be convenient to supply pores, defects and abundant active sites, making it an outstanding substrate. In the final step, the NiO–Pt_{SA}, NiO–$Pt_{cluster}$, and NiO–$Pt_{particle}$ were prepared by immersing porous NiO into the deionized water containing chloroplatinic acid (H_2PtCl_6) solution for spontaneous adsorption. The evolution in the morphology and structure of the different Pt nanostructure decorated catalysts was created by tuning the synthetic reaction time and light condition. No obvious differences and crystal diffraction peaks of Pt for the three catalysts were observed in the XRD patterns, which may be due to the low Pt content (Fig. 1B(III)–(V)). However, the Pt peaks show a gradually increased tendency according to the UV-visible absorption spectra (Fig. 1I), indicating that the Pt content increased in the sequence of NiO–Pt_{SA}, NiO–$Pt_{cluster}$, and NiO–$Pt_{particle}$.

No significant differences were observed in the lamellar morphologies of NiO–Pt_{SA} and NiO–$Pt_{cluster}$ catalysts based on the visualized SEM images (Fig. S6A and S6C†), while the surface of NiO–$Pt_{particle}$ nanoflakes was modified by some small nanoparticles (Fig. S6E†). The high-angle annular dark-field scanning transmission electron microscopy (HAADF-STEM) images (Fig. S6B and S6D†) further confirmed the porous nature of NiO–Pt_{SA} and NiO–$Pt_{cluster}$ nanoflakes. The white highlights recorded in the HAADF-STEM observation of NiO–$Pt_{particle}$ might be ascribed to Pt nanoparticles (Fig. S6F†). The corresponding STEM-EDX maps demonstrated uniform dispersion of Ni and Pt elements throughout NiO nanoflakes. To further confirm the component of light spots, SAED and HRTEM of the three catalysts were conducted, as displayed in Fig. S7–S9,† respectively. The lattice fringes and SAED patterns of NiO–Pt_{SA} and NiO–$Pt_{cluster}$ catalysts matched well with NiO crystals, verifying the substrate as NiO. In contrast, the lattice fringes of 0.22 nm were assigned to the Pt (111) plane for the nanoparticles on the NiO surface, affirming the bright spots as Pt nanoparticles. Additionally, for comparison, pure Pt nanoparticles were fabricated under the same conditions as those for NiO–$Pt_{particle}$ without the addition of NiO (Fig. S10–S12†).

To intuitively investigate the dispersion state of Pt, aberration-corrected high-angle annular darkled-scanning transmission electron microscopy (AC HAADF-STEM) was used to unambiguously contrast the sub-nanometer metal particles. Fig. 2A and B display the AC-HAADF-STEM images of

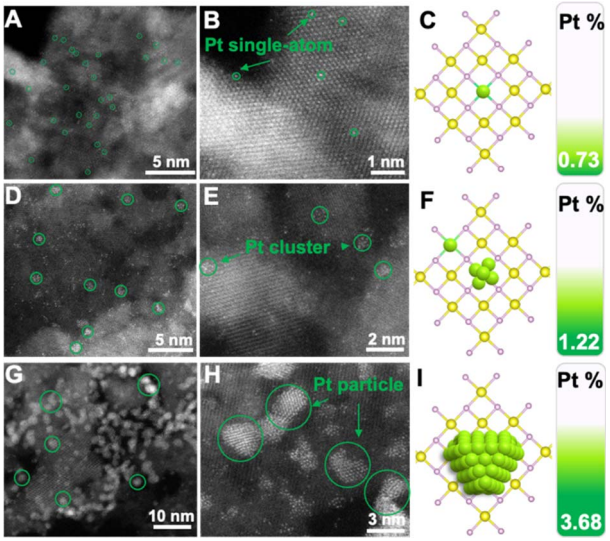

Fig. 2 Atomic structure characterization of the as-prepared NiO–Pt_{SA}, NiO–$Pt_{cluster}$, and NiO–$Pt_{particle}$. (A and B) AC-HAADF-STEM images of NiO–Pt_{SA}. (C) Schematic illustration and ICP-OES of NiO–Pt_{SA}. (D and E) AC-HAADF-STEM images of NiO–$Pt_{cluster}$. (F) Schematic illustration and ICP-OES of NiO–$Pt_{cluster}$. (G and H) AC-HAADF-STEM images of NiO–$Pt_{particle}$. (I) Schematic illustration and ICP-OES of NiO–$Pt_{particle}$.

NiO–Pt_{SA}, showing brighter spots (*i.e.* Pt atoms, marked by the green circles) that were atomically dispersed. Meanwhile, no bright Pt atoms were observed in between any two adjacent lattice fringes, revealing the absence of Pt atoms in the interstitial sites of the lattices. It was thus speculated that Pt atoms substituted Ni sites, *i.e.*, achieved the doping behavior in NiO lattices. The Pt single atom loading was further revealed by ICP-OES as 0.73 wt%, which may change the electronic structure and coordination of the center atoms due to the substitution into the crystal lattices, as illustrated in Fig. 2C. When the Pt loading increased up to 1.22 wt%, not only highly dispersed Pt single atoms but also some bright clusters were found in the AC-HAADF-STEM images of NiO–$Pt_{cluster}$ (Fig. 2D and E), indicating that Pt atoms could be gradually nucleated on the surface of NiO nanoflakes and grew into Pt clusters at such an increased Pt content, as shown in Fig. 2F. In contrast, aggregated spots of ~3 nm were observed in the AC-HAADF-STEM images of NiO–$Pt_{particle}$ with a high Pt loading of 3.68 wt%, corresponding to Pt nanoparticles (Fig. 2G and H). The above results show that Pt may be nucleated from single atoms to nanoparticles through clusters on the surface of NiO nanoflakes, as displayed in Fig. 2I.

The electronic state and chemical composition of the Pt atoms in different NiO/Pt catalysts were investigated by X-ray photoelectron spectroscopy (XPS), as shown in Fig. 3A–C. In Pt 4f spectra, three characteristic states of Pt were deconvoluted, which were ascribed to metallic Pt^0 (70.9 eV, 74.2 eV), Pt^{2+} (72.9 eV, 76.4 eV) and Pt^{4+} (78.35 eV), respectively. In particular, Pt atoms in NiO–Pt_{SA} mainly existed in the valence state of Pt^{2+}, indicating that Pt was coordinated with O in the NiO crystal. Besides the Pt^{2+} coordinations, the signal of metallic Pt^0 was also detected for NiO–$Pt_{cluster}$, indicating that Pt was nucleated

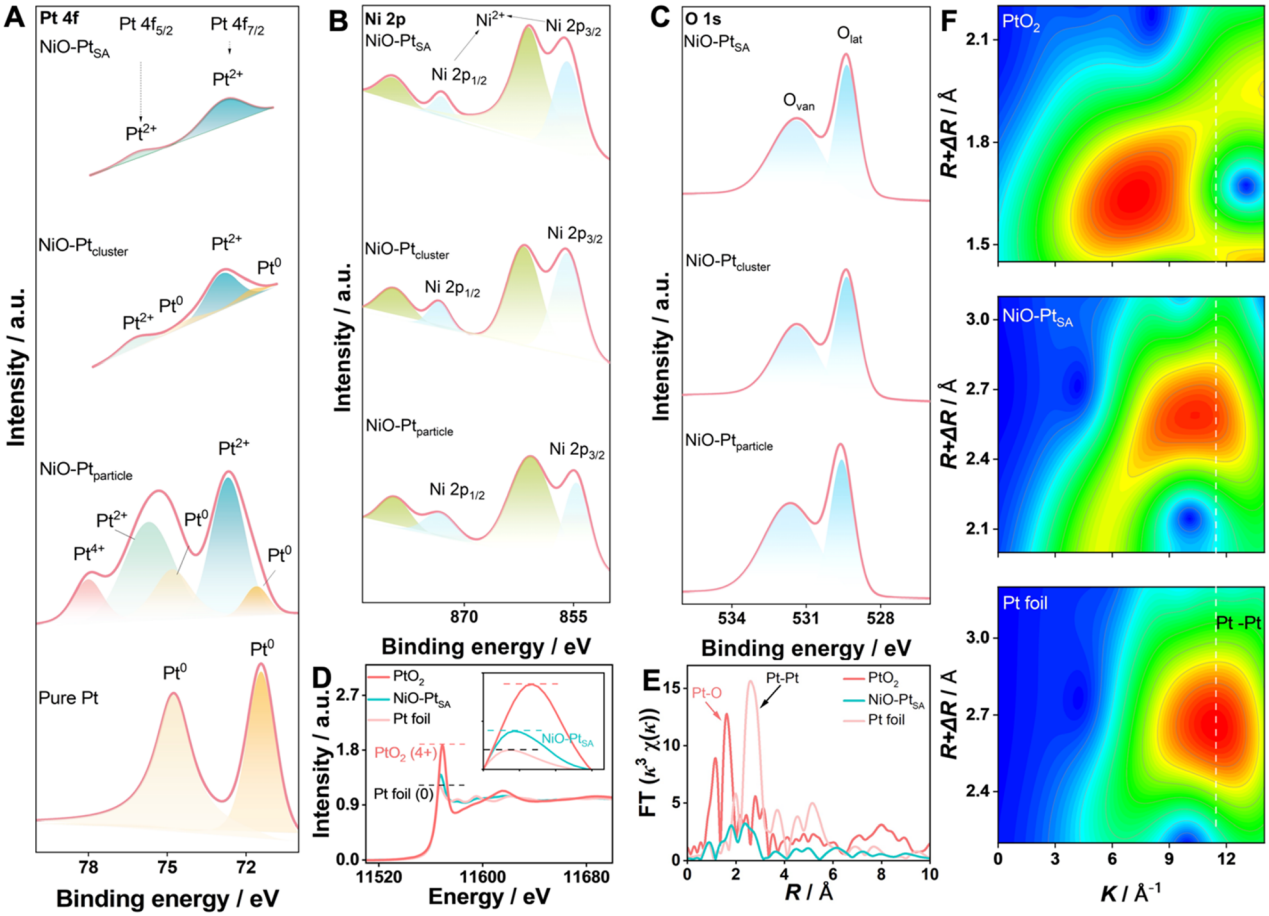

Fig. 3 Electronic state and coordination characterization. XPS spectra of (A) Pt 4f, (B) Ni 2p and (C) O 1s for NiO–Pt_{SA}, NiO–$Pt_{cluster}$, and NiO–$Pt_{particle}$. (D) XANES spectra, (E) the corresponding FT-EXAFS curves and (F) EXAFS wavelet transform plots of NiO–Pt_{SA}, Pt foil and PtO_2.

and grew into clusters. In contrast, the Pt nanoparticles in the NiO–$Pt_{particle}$ catalyst were formed as Pt^0, Pt^{2+} and Pt^{4+} species; herein Pt^{4+} might be derived from the adsorbed $PtCl_6^{2-}$ ions on the surface of the samples.[30,31] The XPS results of Pt were consistent with the AC-HAADF-STEM observations. Fig. 3B depicts the high-resolution Ni 2p spectrum, in which the peaks at 855.8 eV and 873.3 eV along with two weak satellite peaks at 861.0 eV and 879.4 eV corresponded to the Ni $2p_{3/2}$ and Ni $2p_{1/2}$ signals of NiO, respectively. This was assigned to the valence state of Ni^{2+} by forming the Ni–O bond in the NiO crystal. The O 1s spectra of the three catalysts were divided into two characteristic peaks of lattice oxygen (O_{lat}, 529.3 eV) and oxygen vacancies (O_{van}, 532.3 eV), in which the lattice oxygen was formed by M–O (M = Ni and/or Pt) and the oxygen vacancies originate from the porous interfacial defects in the NiO nanoplates.[32]

For the in-depth study of the coordination environment and electronic configuration of Pt single atoms in the NiO–Pt_{SA}, X-ray absorption fine structure (XAFS) spectroscopy was carried out. The Pt L_3-edge normalized X-ray absorption near-edge structure (XANES) spectrum of NiO–Pt_{SA} is significantly distinguished from those of Pt foil and PtO_2 (Fig. 3D), in which the intensity of white-line peaks at 11 568 eV corresponded to the transfer of the Pt $2p_{3/2}$ core electron to 5d states, and thus was used as an indicator of Pt 5d band occupancy.[33,34] The decreased white-line intensity corresponded to the increased Pt 5d occupancy. Thus, lower 5d occupancy indicated the less charge loss of the Pt single atoms after coordinating with the substrate in comparison with Pt foil. This implied that Pt in NiO–Pt_{SA} was positively charged due to the electron transfer from Pt to the surrounding O atoms in the NiO substrate.[24,35] The charge state of Pt in NiO–Pt_{SA} was closely affected by the coordination with the substrate. The atomic coordination configuration of Pt was further revealed by the extended XAFS (EXAFS) at the Pt L_3-edge, as shown in Fig. 3E. The absence of the typical Pt–Pt peak at 2.65 Å for NiO–Pt_{SA} strongly indicated that Pt is in the atomically dispersed single atom state, matching well with the AC-HAADF-STEM observations. Specifically, the dominant peak of Pt–O coordination for NiO–Pt_{SA} slightly shifted to 1.83 Å in comparison with 1.62 Å of PtO_2 in the R-space spectrum, indicating the formed Pt–O as Pt^{2+} instead of Pt^{4+}, which is consistent with the XPS results. As shown in Fig. 3F, the wavelet-transform plots of NiO–Pt_{SA} showed a maximum of about 10.5 Å which was lower than 11.4 Å of Pt foil but higher than 7.4 Å of PtO_2, further confirming the coordination conditions of Pt–O for Pt single atoms in the NiO–Pt_{SA} sample.

The OER electrocatalytic activities of as-fabricated NiO/Pt catalysts were measured in 1.0 M KOH electrolyte, as displayed in Fig. 4. The NiO–Pt_{SA} catalyst possessed the highest OER activity with a rather low overpotential of 0.274 V delivering 10 mA cm^{-2} in comparison with the other catalysts (Fig. 4A). Furthermore, the NiO–Pt_{SA} catalyst exhibited a smaller Tafel slope of 83 mV dec^{-1} and an enhanced double-layer capacitance (C_{dl}) of 58 mF cm^{-2} compared to the hydroxide precursor and the other two NiO/Pt catalysts featuring different Pt nanostructures (Fig. 4B and C), suggesting that atomically dispersed Pt single atoms on the NiO substrate could supply more accessible active sites for the OER. Moreover, when normalized with the Pt loading mass, NiO–Pt_{SA} delivered a higher current of 5.59 A mg_{Pt}^{-1} at an overpotential of 0.274 V, which was 2.64 and 9.63 times that of NiO–$Pt_{cluster}$ (2.11 A mg_{Pt}^{-1}) and NiO–$Pt_{particle}$ (0.58 A mg_{Pt}^{-1}), respectively (Fig. 4D), indicating a much higher mass activity for NiO–Pt_{SA}. The above results highlight that the incorporation of NiO with a minimal amount of Pt single atoms can extremely maximize the mass activity toward alkaline OER, significantly reducing the Pt cost while increasing its utilization. Moreover, the NiO–Pt_{SA} possessed a higher turnover frequency (TOF) and O_2 production rate compared with the other as-prepared catalysts according to the calculations and analyses (Fig. 4E and F). Furthermore, the NiO–Pt_{SA} catalyst demonstrated high durability in continuous electrocatalysis, with negligible potential fluctuation detected over 20 h during the OER at current densities of both 10 mA cm^{-2} and 50 mA cm^{-2} (Fig. 4G). The structural and morphological characterization of the NiO–Pt_{SA} catalyst after the stability test at 10 mA cm^{-2} suggested negligible changes after a long-term alkaline

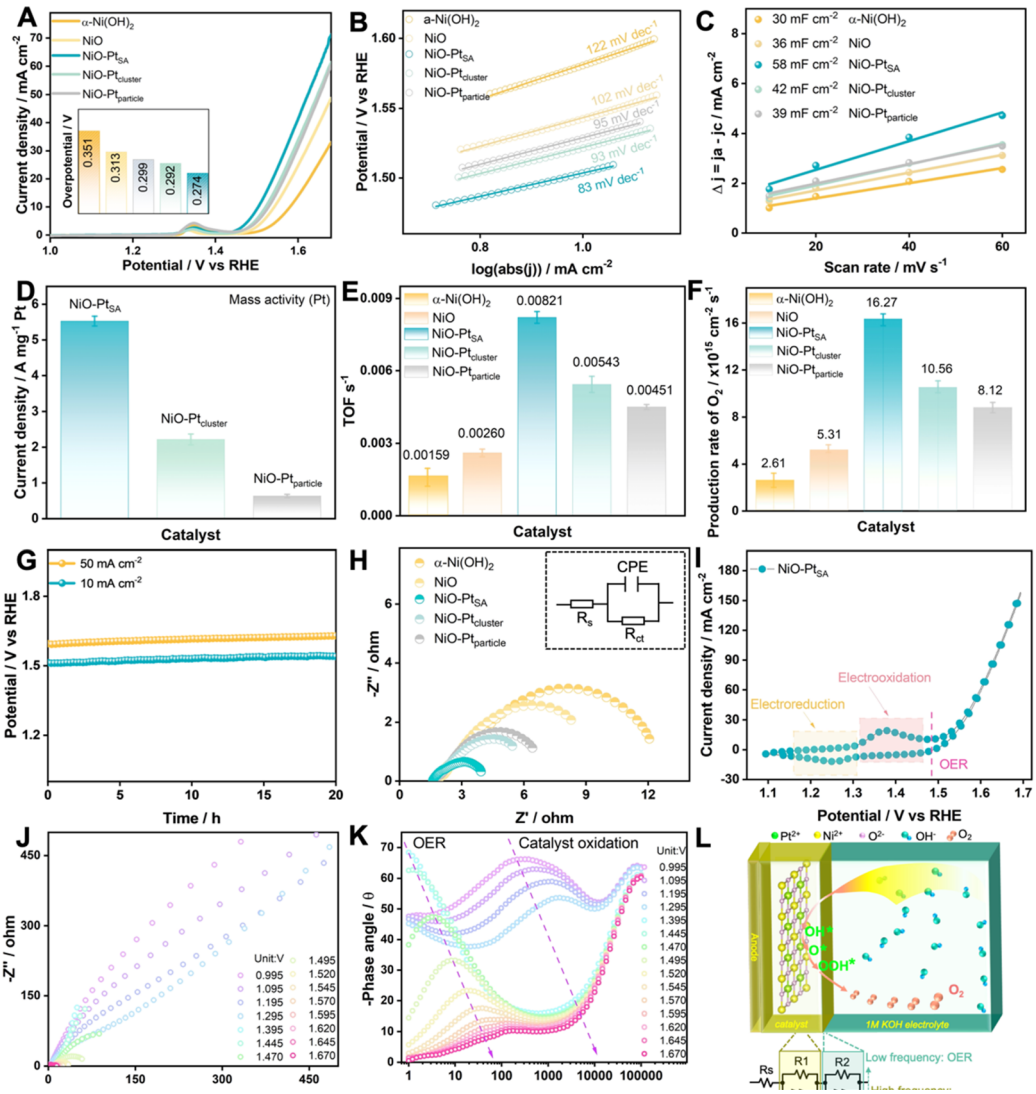

Fig. 4 Electrocatalytic alkaline OER performance of the catalysts in 1.0 M KOH electrolyte. (A) OER polarization curves of α-$Ni(OH)_2$, NiO and kinds of NiO/Pt catalysts, the inset shows the overpotentials of different catalysts delivering a current density of 10 mA cm^{-2}. (B) Tafel slopes. (C) Estimation of C_{dl} by fitting a linear regression at different scan rates. (D) The mass activity of NiO/Pt catalysts. (E) TOFs and (F) production rate of O_2. (G) Chronoamperometric curves of NiO–Pt_{SA}. (H) Nyquist plots of the catalysts, the inset shows the fitting equivalent circuit. (I) CV curve of NiO–Pt_{SA} at 5 mV s^{-1}. (J) Nyquist plots of NiO–Pt_{SA} at different potentials. (K) Bode plots for NiO–Pt_{SA} during the OER. (L) Schematic illustration showing the relationship between surface species, interfaces and reactions for NiO–Pt_{SA} during the OER.

OER process (Fig. S13 and S14†). Meanwhile, the charge transfer resistance (R_{ct}) of NiO–Pt_{SA} was lower than those of precursors and Pt-based catalysts (Fig. 4H and Table S1†), which was mainly due to the optimized electronic structure and coordination environment originating from the atomically Pt dopant in the NiO crystal. Fig. 4I shows the cyclic voltammetry (CV) curve of NiO–Pt_{SA}, in which a pair of redox peaks were observed before the OER region, revealing that the catalyst was electro-oxidized before the OER process. To probe the interface electron transfer reactions, *operando* EIS was conducted to obtain the Nyquist (Fig. 4J) and Bode plots (Fig. 4K) during the OER for NiO–Pt_{SA}. The charge transfer resistance significantly decreased with the increase of potential, accompanied by distinct electro–oxidation reaction and OER. The equivalent circuit diagram and model, as presented in Fig. 4L, represent the situations before and/or after electro–oxidation reaction.[36,37] Based on the intrinsic consistency of the equivalent resistance with the reaction and current density of the NiO–Pt_{SA} catalyst, it was speculated that the electro-oxidation reaction (in the potential windows higher than 1.295 V) took place at the high-frequency interface while the OER (in the potential region higher than 1.470 V) occurred at the low-frequency interface.

To deeply understand the structural transition during the OER, *in situ* Raman electrochemical investigation was conducted on NiO–Pt_{SA} during the overpotential sweep from 0 to 400 mV (Fig. 5A). Five characteristic peaks appeared at 539, 735, 909, 1091 and 1507 cm^{-1} under no bias condition, which match well with the first-order longitudinal optical (LO), transverse optical (2TO), LO+TO, 2LO and 2 M modes of NiO, respectively.[38,39] At an overpotential of 0 V (1.23 V *vs.* RHE), additional peaks slightly appeared at 477 and 558 cm^{-1}, corresponding to the γ-NiOOH phase.[40,41] With increased overpotentials, the signal intensity of γ-NiOOH intensified, while that for NiO decreased, verifying that introducing Pt single atoms facilitates a structural transition at a lower potential and plays the key role in boosting subsequent OER kinetics.

XPS was engaged to analyze the surface chemical states and element components of NiO–Pt_{SA} after the OER stability test (Fig. 5B and S15†). The survey XPS spectrum identified Ni, Pt, C and O with 11.18, 0.03, 43.00 and 45.8 at%, respectively (the inset of Fig. 5B). Accordingly, the proportions of Pt and Ni were 0.35 at% and 99.65 at% (Table S2†), respectively, indicating that the Pt content did not show significant loss after OER measurement compared to that in the initial catalyst (0.73 wt%, 0.34 at%). The O 1s spectrum still exhibited two peaks for the oxygen lattice and vacancies, respectively. The Ni 2p spectrum also deconvoluted to two sets of Ni $2p_{3/2}$ and Ni $2p_{1/2}$ assigned to Ni^{2+}, indicating that the structural transformation of the NiOOH phase into initial NiO is highly reversible. The Pt 4f spectrum was assigned to Pt^{2+} without any other peaks, indicating that Pt single atoms are relatively robust and no agglomeration occurs due to the absence of metallic Pt peaks after the OER.

The energy barrier is a key descriptor to evaluate the rate-determining step for the OER. Density functional theory (DFT) calculations were introduced to calculate the Gibbs free energy on different active sites for pure NiO, NiO–Pt_{SA}, and NiO–$Pt_{cluster}$. Fig. S16† exhibits the intermediate transformation pathway (OH*, O* and OOH*) in the OER process for Ni sites of the pure NiO catalyst, through which the rate-determining step of pure NiO was determined as the deprotonation of OH*. Moreover, the reaction dynamics on the Ni and Pt active sites of NiO–Pt_{SA} were further investigated (Fig. 5C–E). The rate-determining step was ascribed to the adsorption of OH* to form OOH* with an energy

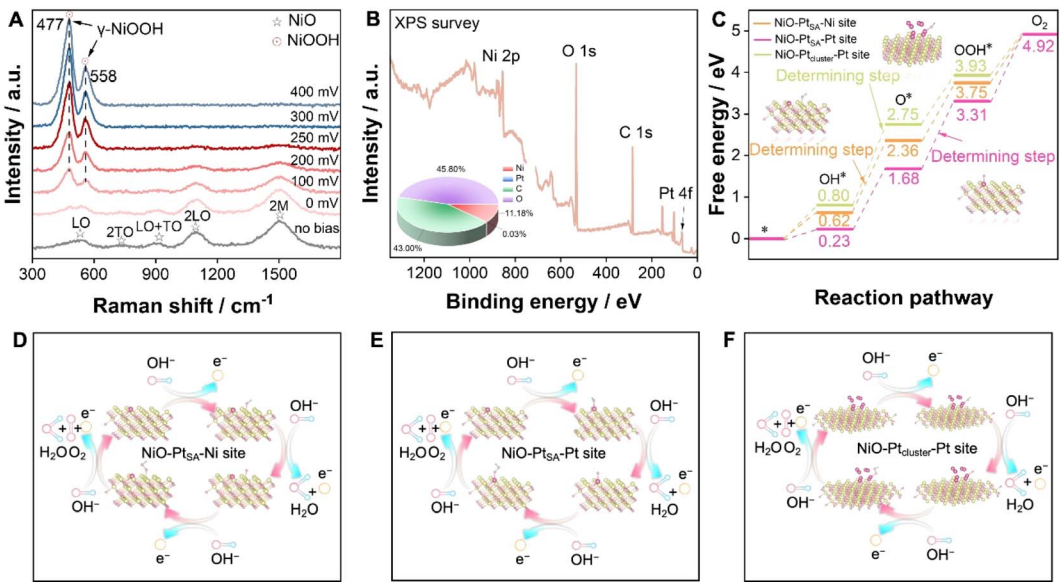

Fig. 5 Mechanism and theoretical calculations on the OER. (A) The *in situ* Raman spectra of NiO–Pt_{SA} under various applied overpotentials. (B) The survey XPS of NiO–Pt_{SA} after the OER stability test. The inset is the atomic content of Ni, Pt, C and O in the NiO–Pt_{SA} catalyst after the OER stability test, obtained from the XPS. (C) Free energy diagrams. Reaction pathways for the OER on the (D) Ni site in NiO–Pt_{SA}, (E) Pt site in NiO–Pt_{SA} and (F) Pt site in NiO–$Pt_{cluster}$.

barrier of 1.62 eV on the Pt sites of NiO–Pt_{SA} for the OER, which was lower than 1.75 eV for the deprotonation of OH* on Ni sites, indicating that Pt single atoms in NiO–Pt_{SA} tended to be the active sites for the OER and were more favorable for O_2 generation. When the Pt atoms aggregated into a cluster state, the rate-determining step of the NiO–$Pt_{cluster}$ on Pt sites changed back to the deprotonation of OH* with an energy barrier of 1.95 eV (Fig. 5C and F), which was higher than the Pt single atom state, suggesting that the Pt clusters might be less conducive to the OER process. Therefore, it could be concluded that tunable metal–support interactions originating from the size and dispersion of Pt directly affected the OER process. In particular, Pt single atoms in NiO nanoflakes reduced the energy barrier and thus promoted the OER process.

The MOR performance of the as-prepared catalysts was tested in a mixed 1.0 M KOH + 1.0 M CH_3OH aqueous electrolyte. The catalytic activities were evaluated from CV curves at a scan rate of 50 mV s^{-1}, as recorded in Fig. 6A and S17.† Pure NiO exhibited no obvious current response toward the MOR, while all three NiO/Pt catalysts showed a significant current increase when using NiO as the substrate. The NiO–Pt_{SA} catalyst displayed the lowest onset oxidation potential (0.519 V *vs.* RHE) compared with NiO–$Pt_{cluster}$ (0.541 V *vs.* RHE) and NiO–$Pt_{particle}$ (0.615 V *vs.* RHE), indicating that Pt single atoms enabled NiO–Pt_{SA} to be an efficient MOR electrocatalyst compared to the other catalysts. The lowest onset oxidation potential of NiO–Pt_{SA} revealed the formation of weakly adsorbed CO_{ads} on Ni and/or Pt active sites, which affected the key step of the co-adsorption of *CO + *OH in the MOR to avoid self-poisoning and deactivation of the catalyst.[42,43] In addition, the ratios of the forward peak current density (I_f) to backward peak current density (I_b), *i.e.* I_f/I_b, were estimated to be 5.13, 4.30, 3.52, and 1.93 for NiO–Pt_{SA}, NiO–$Pt_{cluster}$, NiO–$Pt_{particle}$ and pure Pt catalysts, respectively. The prominent I_f/I_b of NiO–Pt_{SA} indicated a more efficient MOR process with less residual intermediate species which were generated as a result of the incomplete electrooxidation of CH_3OH. Moreover, as presented in Fig. 6B, the mass activity of NiO–Pt_{SA} (0.422 A mg_{Pt}^{-1}) was 2.62 and 18.35 times that of NiO–$Pt_{cluster}$ (0.161 A mg_{Pt}^{-1}) and NiO–$Pt_{particle}$ (0.023 A mg_{Pt}^{-1}), respectively. Higher peak mass activity and smaller peak potential of NiO–Pt_{SA} indicated a lower activation barrier. Such a prominent mass activity was also superior to those of previously reported Pt-based catalysts.[44–49] The effect of I_b on methanol oxidation was assessed by comparing the typical forward direction with the reverse direction (Fig. 6C). Two curves were highly overlapped, which revealed that backward oxidation was almost not influenced by the forward or reverse reactions. The EIS data, as shown in Fig. 6D and Table S3,† indicated that NiO–Pt_{SA} presented a smaller semicircle radius of impedance than those of NiO–$Pt_{cluster}$ and NiO–$Pt_{particle}$, which implied that electron transfer was significantly facilitated because of the Pt single atoms–NiO support interaction. Chronoamperometry was carried out at 0.70 V *vs.* RHE to further evaluate the durability toward the MOR (Fig. 6E). It should be noted that the final current density of NiO–Pt_{SA} after 10 000 s was remarkedly higher than those of NiO–$Pt_{cluster}$ and NiO–$Pt_{particle}$. In addition, NiO–Pt_{SA} maintained a superior capacity retention of 95% after 500 cycles for the MOR (Fig. S18†). The outstanding electrocatalytic stability and

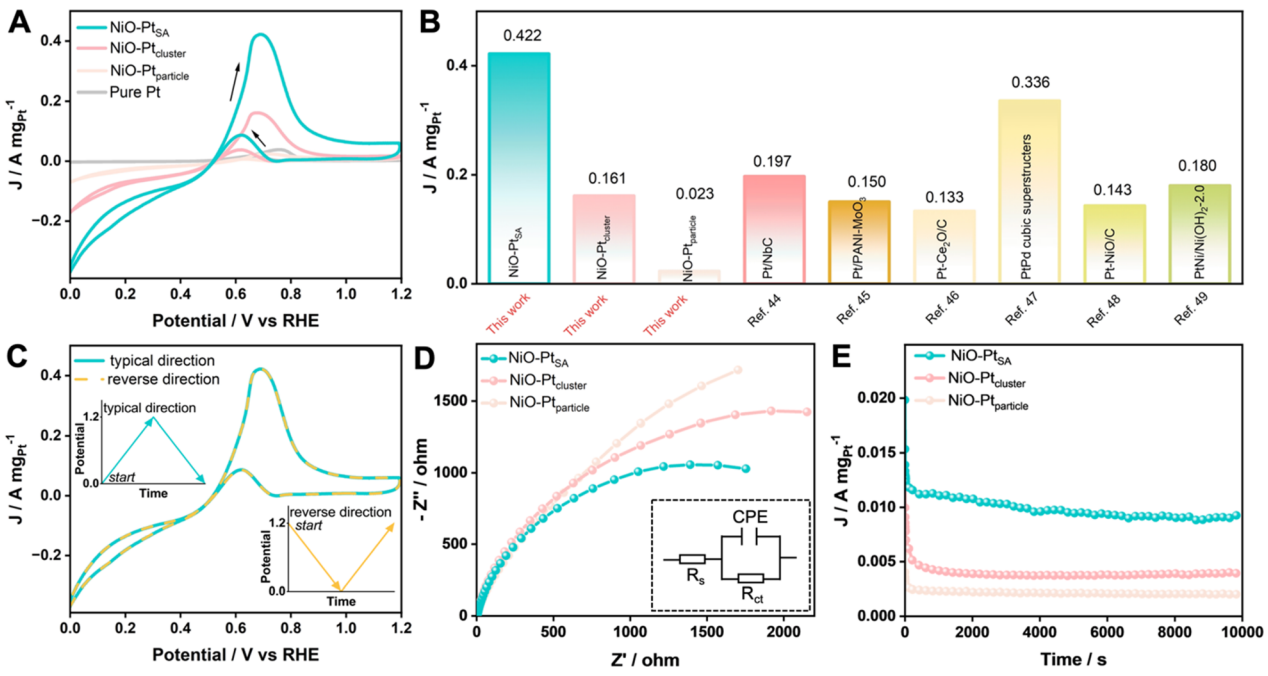

Fig. 6 MOR performance in a mixed electrolyte of 1.0 M KOH and 1.0 M CH_3OH. (A) The mass-normalized CV curves and (B) a comparison showing mass activities at peak potentials for as-prepared catalysts at 50 mV s^{-1} and the previously reported Pt-based catalysts. (C) CV results of NiO–Pt_{SA} with the typical direction and reverse direction (blue line: typical direction, yellow dashed line: reverse direction). (D) Nyquist plots, the inset shows the simulated circuit. (E) Chronoamperometry curves for the NiO/Pt catalysts at 0.70 V for 10 000 s.

durability of the NiO–Pt_{SA} further verified its excellent anti-poisoning properties.

Conclusions

A series of NiO/Pt catalysts with different Pt nanostructures (single atoms, clusters, and nanoparticles) were prepared using a simple adsorption–impregnation strategy by adjusting the light condition and reaction prolongation, and further applied to the electrocatalytic OER and MOR. According to experimental analyses and theoretical calculations, Pt single atoms in the Pt^{2+} valence state are mainly coordinated with the surrounding O, optimizing the electronic structure and coordination of the metal centers, *i.e.* the metal–support interactions. This strategy combined the advantages of porous nanoflake structures of the NiO substrate with the Pt dopant to optimize the noble metal–NiO support interactions. As a result, the NiO–Pt_{SA} catalyst showed the merits of low Pt loading for high Pt utilization, and improved transmission of active species with a remarkably enhanced catalytic activity of 5.59 A mg_{Pt}^{-1} for the OER and 0.42 A mg_{Pt}^{-1} for the MOR, which significantly surpassed the NiO–$Pt_{cluster}$ and NiO–$Pt_{particle}$. This work will offer an approach of carefully modulating metal–non-carbon support interactions to develop highly active hybrid catalysts for energy-related technologies.

Data availability

The theoretical calculations and experimental procedure details have been provided within the manuscript and ESI.† The data that support the findings of this study are available from the corresponding authors upon reasonable request.

Author contributions

F. W. and H. W. conceived and coordinated the project. H. W., G. C., N. Z., X. L., and R. M. supervised the project. F. W. performed the experiments, analyzed the data, and wrote the original draft. Z. Z. assisted with the DFT calculations and analysis. D. W. helped with the OER measurements and data analyses. The manuscript was finished through the contributions of all authors. All authors have approved the final version of the manuscript.

Conflicts of interest

The authors declare no competing financial interest.

Acknowledgements

This work is financially supported by the National Natural Science Foundation of China (U20A20123 and 51874357). H. W. acknowledges the support from the Project of Zhongyuan Critical Metals Laboratory (GJJSGFYQ202336). This work was supported in part by the High-Performance Computing Center of Central South University.

Notes and references

1 Z. X. Xia, X. M. Zhang, H. Sun, S. L. Wang and G. Q. Sun, Recent advances in multi-scale design and construction of materials for direct methanol fuel cells, *Nano Energy*, 2019, **65**, 104048.
2 H. Chen, J. Chen, P. Ning, X. Chen, J. Liang, X. Yao, D. Chen, L. Qin, Y. Huang and Z. Wen, 2D Heterostructure of Amorphous CoFeB Coating Black Phosphorus Nanosheets with Optimal Oxygen Intermediate Absorption for Improved Electrocatalytic Water Oxidation, *ACS Nano*, 2021, **15**, 12418–12428.
3 E. Sarwar, T. Noor, N. Iqbal, Y. Mehmood, S. Ahmed and R. Mehek, Effect of Co-Ni Ratio in Graphene Based Bimetallic Electro-catalyst for Methanol Oxidation, *Fuel Cells*, 2018, **18**, 189–194.
4 A. Carne-Sanchez, F. J. Carmona, C. Kim and S. Furukawa, Porous materials as carriers of gasotransmitters towards gas biology and therapeutic applications, *Chem. Commun.*, 2020, **56**, 9750–9766.
5 C. Liu, Y. Shen, J. F. Zhang, G. Li, X. R. Zheng, X. P. Han, L. Y. Xu, S. Z. Zhu, Y. A. Chen, Y. D. Deng and W. B. Hu, Multiple Twin Boundary-Regulated Metastable Pd for Ethanol Oxidation Reaction, *Adv. Energy Mater.*, 2022, **12**, 2103505.
6 Y. W. Zhou, Y. F. Chen, K. Jiang, Z. Liu, Z. J. Mao, W. Y. Zhang, W. F. Lin and W. B. Cai, Probing the enhanced methanol electrooxidation mechanism on platinum-metal oxide catalyst, *Appl. Catal., B*, 2021, **280**, 119393.
7 W. C. Geng, Y. J. Zhang, L. Yu, J. J. Li, J. L. Sang and Y. J. Li, Integrating Pt(16) Te Nanotroughs and Nanopillars into a 3D "Self-Supported" Hierarchical Nanostructure for Boosting Methanol Electrooxidation, *Small*, 2021, **17**, e2101499.
8 L. L. Zhang, P. P. Lu, Y. R. Luo, J. Y. Zheng, W. Ma, L. X. Ding and H. H. Wang, Graphene-quantum-dot-composited platinum nanotube arrays as a dual efficient electrocatalyst for the oxygen reduction reaction and methanol electrooxidation, *J. Mater. Chem. A*, 2021, **9**, 9609–9615.
9 X. M. Zhao, X. Liu, B. Y. Huang, P. Wang and Y. Pei, Hydroxyl group modification improves the electrocatalytic ORR and OER activity of graphene supported single and bi-metal atomic catalysts (Ni, Co, and Fe), *J. Mater. Chem. A*, 2019, **7**, 24583–24593.
10 L. Bu, N. Zhang, S. Guo, X. Zhang, J. Li, J. Yao, T. Wu, G. Lu, J. Y. Ma, D. Su and X. Huang, Biaxially strained PtPb/Pt core/shell nanoplate boosts oxygen reduction catalysis, *Science*, 2016, **354**, 1410–1414.
11 X. Li, C. Deng, Y. Kong, Q.-H. Huo, L.-R. Mi, J.-J. Sun, J.-Y. Cao, J.-X. Shao, X.-B. Chen, W.-L. Zhou, M.-Y. Lv, X.-Y. Chai, H.-P. Yang, Q. Hu and C.-X. He, Unlocking the transition of electrochemical water oxidation mechanism induced by heteroatom doping, *Angew. Chem., Int. Ed.*, 2023, **62**, e202309732.
12 Z. Zhang, J. Liu, J. Wang, Q. Wang, Y. Wang, K. Wang, Z. Wang, M. Gu, Z. Tang, J. Lim, T. Zhao and F. Ciucci,

Single-atom catalyst for high-performance methanol oxidation, *Nat. Commun.*, 2021, **12**, 5235.

13 X.-J. Li, H.-K. Zhang, Q. Hu, W.-L. Zhou, J.-X. Shao, X.-X.-X. Jiang, C. Feng, H.-P. Yang and C.-X. He, Amorphous NiFe oxide-based nanoreactors for efficient electrocatalytic water oxidation, *Angew. Chem., Int. Ed.*, 2023, **62**, e202300478.

14 K. Jiang, B. Liu, M. Luo, S. Ning, M. Peng, Y. Zhao, Y. R. Lu, T. S. Chan, F. M. F. de Groot and Y. Tan, Single platinum atoms embedded in nanoporous cobalt selenide as electrocatalyst for accelerating hydrogen evolution reaction, *Nat. Commun.*, 2019, **10**, 1743.

15 Q. Hu, K.-R. Gao, X.-D. Wang, H.-G. Zheng, J.-Y. Cao, L.-R. Mi, Q.-H. Huo, H.-P. Yang, J.-H. Liu and C.-X. He, Subnanometric Ru clusters with upshifted D band center improve performance for alkaline hydrogen evolution reaction, *Nat. Commun.*, 2022, **13**, 3958.

16 F. Kong, X. Liu, Y. Song, Z. Qian, J. Li, L. Zhang, G. Yin, J. Wang, D. Su and X. Sun, Selectively Coupling Ru Single Atoms to PtNi Concavities for High-Performance Methanol Oxidation via d-Band Center Regulation, *Angew. Chem., Int. Ed.*, 2022, **61**, e202207524.

17 Y. N. Gong, L. Jiao, Y. Qian, C. Y. Pan, L. Zheng, X. Cai, B. Liu, S. H. Yu and H. L. Jiang, Regulating the Coordination Environment of MOF-Templated Single-Atom Nickel Electrocatalysts for Boosting CO_2 Reduction, *Angew. Chem., Int. Ed.*, 2020, **59**, 2705–2709.

18 R. Qin, K. Liu, Q. Wu and N. Zheng, Surface Coordination Chemistry of Atomically Dispersed Metal Catalysts, *Chem. Rev.*, 2020, **120**, 11810–11899.

19 C. Tang, Y. Jiao, B. Shi, J. N. Liu, Z. Xie, X. Chen, Q. Zhang and S. Z. Qiao, Coordination Tunes Selectivity: Two-Electron Oxygen Reduction on High-Loading Molybdenum Single-Atom Catalysts, *Angew. Chem., Int. Ed.*, 2020, **59**, 9171–9176.

20 Q. Hu, S. Qi, Q.-H. Huo, Y.-X. Zhao, J.-J. Sun, X.-B. Chen, M.-Y. Lv, W.-L. Zhou, C. Feng, X.-Y. Chai, H.-P. Yang and C.-X. He, Designing efficient nitrate reduction electrocatalysts by identifying and optimizing active sites of Co-based spinels, *J. Am. Chem. Soc.*, 2024, **146**, 2967–2976.

21 Z.-Y. He, J. Zhang, Z.-L. Gong, H. Lei, D. Zhou, N. Zhang, W.-J. Mai, S.-J. Zhao and Y. Chen, Activating lattice oxygen in NiFe-based (oxy) hydroxide for water electrolysis, *Nat. Commun.*, 2022, **13**, 2191.

22 Y. T. Kim, K. Ohshima, K. Higashimine, T. Uruga, M. Takata, H. Suematsu and T. Mitani, Fine size control of platinum on carbon nanotubes: from single atoms to clusters, *Angew. Chem., Int. Ed.*, 2006, **45**, 407–411.

23 Y. Ding, B. Q. Miao, Y. C. Liu, N. Hou, Y. Yang, P. J. Jin, S. B. Yin and Y. Chen, Rhodium-Cobalt Alloy Nanotubes Toward Methanol Oxidation Reaction, *Small Struct.*, 2022, **3**, 2200046.

24 J. Q. Zhang, Y. F. Zhao, X. Guo, C. Chen, C. L. Dong, R. S. Liu, C. P. Han, Y. D. Li, Y. Gogotsi and G. X. Wang, Single platinum atoms immobilized on an MXene as an efficient catalyst for the hydrogen evolution reaction, *Nat. Catal.*, 2018, **1**, 985–992.

25 D. B. Liu, X. Y. Li, S. M. Chen, H. Yang, C. D. Wang, C. Q. Wu, Y. A. Haleem, S. Duan, J. L. Lu, B. H. Ge, P. M. Ajayan, Y. Luo, J. Jiang and L. Song, Atomically dispersed platinum supported on curved carbon supports for efficient electrocatalytic hydrogen evolution, *Nat. Energy*, 2019, **4**, 512–518.

26 L. Hui, Y. R. Xue, C. Y. Xing, Y. X. Liu, Y. C. Du, Y. Fang, H. D. Yu, C. Zhang, F. He and Y. L. Li, Atomic alloys of nickel-platinum on carbon network for methanol oxidation, *Nano Energy*, 2022, **95**, 106984.

27 C. Lin, Y. Zhao, H. Zhang, S. Xie, Y. F. Li, X. Li, Z. Jiang and Z. P. Liu, Accelerated active phase transformation of NiO powered by Pt single atoms for enhanced oxygen evolution reaction, *Chem. Sci.*, 2018, **9**, 6803–6812.

28 Y. T. Kim, K. Ohshima, K. Higashimine, T. Uruga, M. Takata, H. Suematsu and T. Mitani, Fine size control of platinum on carbon nanotubes: from single atoms to clusters, *Angew. Chem., Int. Ed.*, 2006, **45**, 407–411.

29 B. D. McNicol, Electrocatalytic problems associated with the development of direct methanol-air fuel cells, *J. Electroanal. Chem. Interfacial Electrochem.*, 1981, **118**, 71–87.

30 K. L. Zhou, C. Wang, Z. Wang, C. B. Han, Q. Zhang, X. Ke, J. Liu and H. Wang, Seamlessly conductive $Co(OH)_2$ tailored atomically dispersed Pt electrocatalyst with a hierarchical nanostructure for an efficient hydrogen evolution reaction, *Energy Environ. Sci.*, 2020, **13**, 3082–3092.

31 A. Romanchenko, M. Likhatski and Y. Mikhlin, X-ray Photoelectron Spectroscopy (XPS) Study of the Products Formed on Sulfide Minerals Upon the Interaction with Aqueous Platinum (IV) Chloride Complexes, *Minerals*, 2018, **8**, 578.

32 L. Cao, Q. Luo, J. Chen, L. Wang, Y. Lin, H. Wang, X. Liu, X. Shen, W. Zhang, W. Liu, Z. Qi, Z. Jiang, J. Yang and T. Yao, Dynamic oxygen adsorption on single-atomic Ruthenium catalyst with high performance for acidic oxygen evolution reaction, *Nat. Commun.*, 2019, **10**, 4849.

33 N. Cheng, S. Stambula, D. Wang, M. N. Banis, J. Liu, A. Riese, B. Xiao, R. Li, T. K. Sham, L. M. Liu, G. A. Botton and X. Sun, Platinum single-atom and cluster catalysis of the hydrogen evolution reaction, *Nat. Commun.*, 2016, **7**, 13638.

34 S. Dai, J. P. Chou, K. W. Wang, Y. Y. Hsu, A. Hu, X. Pan and T. Y. Chen, Platinum-trimer decorated cobalt-palladium core-shell nanocatalyst with promising performance for oxygen reduction reaction, *Nat. Commun.*, 2019, **10**, 440.

35 J. Zhang, T. Wang, P. Liu, Z. Liao, S. Liu, X. Zhuang, M. Chen, E. Zschech and X. Feng, Efficient hydrogen production on $MoNi_4$ electrocatalysts with fast water dissociation kinetics, *Nat. Commun.*, 2017, **8**, 15437.

36 R. L. Doyle and M. E. G. Lyons, Kinetics and Mechanistic Aspects of the Oxygen Evolution Reaction at Hydrous Iron Oxide Films in Base, *J. Electrochem. Soc.*, 2013, **160**, H142–H154.

37 M. E. Lyons, R. L. Doyle and M. P. Brandon, Redox switching and oxygen evolution at oxidized metal and metal oxide electrodes: iron in base, *Phys. Chem. Chem. Phys.*, 2011, **13**, 21530–21551.

38 L. Zhao, Y. Zhang, Z.-L. Zhao, Q.-H. Zhang, L.-B. Huang, L. Gu, G. Lu, J.-S. Hu and L.-J. Wan, Steering elementary steps towards efficient alkaline hydrogen evolution via size-dependent Ni/NiO nanoscale heterosurfaces, *Natl. Sci. Rev.*, 2020, **7**, 27–36.

39 J. Al Boukhari, M. Noun and R. Awad, Raman spectroscopic investigations of pure, (Mg, Cu), and (Mg, Ru) codoped NiO nanoparticles, *Chem. Phys. Lett.*, 2024, **836**, 141038.

40 M. Liu, K.-A. Min, B. Han and L. Y. S. Lee, Interfacing or doping? Role of Ce in highly promoted water oxidation of NiFe-layered double hydroxide, *Adv. Energy Mater.*, 2021, **11**, 2101281.

41 Z. Qiu, C.-W. Tai, G.-A. Niklasson and T. Edvinsson, Direct observation of active catalyst surface phases and the effect of dynamic self-optimization in NiFe-layered double hydroxides for alkaline water splitting, *Energy Environ. Sci.*, 2019, **12**, 572–581.

42 D.-J. Chen and Y.-J. Tong, Irrelevance of carbon monoxide poisoning in the methanol oxidation reaction on a PtRu electrocatalyst, *Angew. Chem., Int. Ed.*, 2015, **54**, 9394–9398.

43 Q. Lu, X. Zhao, R. Luque and K. Eid, Structure-activity relationship of tri-metallic Pt-based nanocatalysts for methanol oxidation reaction, *Coord. Chem. Rev.*, 2023, **493**, 215280.

44 O.-T. Ajenifujah, A. Nouralishahi, S. Carl, S.-C. Eady, Z. Jiang and L.-T. Thompson, Platinum supported on early transition metal carbides: efficient electrocatalysts for methanol electro-oxidation reaction in alkaline electrolyte, *Chem. Eng. J.*, 2021, **406**, 126670.

45 Q. Zhang, J.-N. Lv, X.-Y. Hu, Y.-L. He, H.-F. Yang, D.-S. Kong and Y.-Y. Feng, Polyaniline decorated MoO_3 nanorods: synthesis, characterization and promoting effect to Pt electrocatalyst, *Int. J. Hydrogen Energy*, 2018, **43**, 5603–5609.

46 C. Xu, R. Zeng, P.-K. Shen and Z. Wei, Synergistic effect of CeO_2 modified Pt/C catalysts on the alcohols oxidation, *Electrochim. Acta*, 2005, **51**, 1031–1035.

47 L. N. Zhou, X. T. Zhang, Z. H. Wang, S. Guo and Y. J. Li, Cubic superstructures composed of PtPd alloy nanocubes and their enhanced electrocatalysis for methanol oxidation, *Chem. Commun.*, 2016, **52**, 12737–12740.

48 P.-K. Shen, C. Xu, R. Zeng and Y. Liu, Electro-oxidation of methanol on NiO-promoted Pt/C and Pd/C catalysts, *Electrochem. Solid-State Lett.*, 2005, **9**, A39.

49 K.-M. Yu, G.-Q. Ning, J.-T. Yang, Y. Wang, X. Zhang, Y.-C. Qin, C.-L. Luan, L. Yu, Y. Jiang, X.-B. Luan, Z. Dong, H. Wang and X.-P. Dai, Restructured PtNi on ultrathin nickel hydroxide for enhanced performance in hydrogen evolution and methanol oxidation, *J. Catal.*, 2019, **375**, 267–278.